2015

Terahertz Radiation from High-Temperature Superconducting BSCCO Mesas of Various Geometries

Daniel P. Cerkoney
University of Central Florida

TERAHERTZ RADIATION FROM HIGH-TEMPERATURE SUPERCONDUCTING BSCCO MESAS OF VARIOUS GEOMETRIES

by

DANIEL P. CERKONEY

A thesis submitted in partial fulfilment of the requirements
for the Honors in the Major Program in Physics
in the College of Sciences
and in the Burnett Honors College
at the University of Central Florida
Orlando, Florida

Fall Term 2015

Thesis Chair: Richard Klemm, Ph.D

ABSTRACT

The purpose of this thesis is to examine the radiation from high-temperature superconducting mesas of $\mathrm{Bi_2Sr_2CaCu_2O_{8+\delta}}$ (BSCCO). This is motivated by the need for coherent sources of continuous wave terahertz (THz) emission capable of radiating practically in the THz frequency band. As BSCCO has been shown to be tunable from 0.5–2.4 THz (i.e., through the entire so-called terahertz gap centered about 1 THz), and has a higher peak operating temperature near 1 THz than most alternative sources, it is a good candidate for imaging and spectroscopy device applications [1]. When a static DC voltage is applied to a BSCCO mesa, the stack of Josephson junctions intrinsic to this type-II layered superconductor synchronously radiate. Adjustment of the bath temperature and applied voltage allows for the high degree of tunability observed for such an emitter [2]. To determine the angular dependence of radiation from BSCCO mesas, the dual source model from antenna theory is employed, and Love's equivalence principle is used to simplify this framework. The total emission power obtained in this manner for the pie-shaped wedge is then fit to experimental results for a thin isosceles triangular mesa using the method of least squares, resulting in a standard deviation of $\sigma = 0.4657$. Additionally, symmetry is shown to play a significant role in the emissions for the transverse magnetic (TM) cavity modes of the equilateral triangular mesa. When the full group symmetry is imposed, the density of allowed modes is heavily diminished, and the original first excited even mode becomes the C_{3v} symmetric ground state. These results for the equilateral triangle suggest, along with earlier experiments on the regular pentagonal mesa [3], that symmetry breaking effects can be used for purposes of tuning the characteristic frequency and angular dependence of the power radiated from BSCCO mesas with a high degree of symmetry.

ACKNOWLEDGMENTS

I wish to thank Dr. Richard Klemm for his guidance in the development of this thesis, and for being an irreplaceable mentor over the course of my undergraduate career. I am glad that I could contribute to this rapidly evolving field of research; it has truly been a pleasure working with you.

TABLE OF CONTENTS

LIST OF FIGURES

LIST OF TABLES

CHAPTER 1: INTRODUCTION

In recent decades, there has been considerable interest in finding coherent sources of radiation in the terahertz (THz) frequency range. From the standpoint of engineering convenient devices for radiation emission and detection, the band of frequencies roughly centered about 1 THz (appropriately coined the *terahertz gap*) has proved elusive for some time. This region lies between the radio and infrared frequencies, and as a result, typical solid-state emitters such as resonant-tunneling diodes and quantum cascade lasers have difficulty bridging the THz gap completely.

When resonant-tunneling diodes are pushed to frequencies beyond about 1.4 THz [2], the output power falls off quickly, and is generally of the microwatt order [6]. Likewise, while quantum cascade lasers are quite capable of radiating with output powers in the milliwatt range between roughly 1–5 THz, the peak operating temperature and power fall off quickly with decreasing frequency.

For example, while a continuous wave quantum cascade laser has been tuned to 0.84 THz, the operating temperature was 40 K, and the emission power was less than 1 mW [13]. So, while these two solid-state devices can cover the THz range disjointedly, a practical device capable of coherent continuous wave emission near the center of the THz gap is highly desirable.

The layered superconductor $\mathrm{Bi_2Sr_2CaCu_2O_{8+\delta}}$ provides a viable means of spanning the THz gap. Perhaps more importantly, the radiation from superconducting BSCCO mesas is highly tunable and coherent [11, 12]. That is, with proper adjustment of the bath temperature of the mesa and the applied DC voltage, the characteristic frequency of emission/detection can be precisely altered. In fact, recent experiments have shown a cylindrical stand-alone mesa of BSCCO tunable over the entire terahertz gap, specifically, from 0.5–2.4 THz [1]. These properties make a BSCCO emitter a good candidate device for ultrafast communications, imaging and spectroscopy in the THz regime.

In this thesis, the effects of the geometry of a BSCCO mesa on the emission spectrum will be examined by determining the angular dependence of radiation. To this end, a phenomenological model of the radiation due to the (intrinsically nonlinear) AC Josephson current must be implemented, specifically, the dual source radiation model to be discussed in Chapter 2. Experimental data for the radiation intensity of an acute isosceles triangular mesa is then fit with this model via approximation by a thin wedge.

The equilateral triangular mesa geometry could lend itself more to scalability than the previously studied circular and rectangular mesas, as more compact arrays can be built [8, 16]. Some novel implications of symmetry considerations on the cavity mode radiation from equilateral triangular mesas will also be discussed in detail, and it will be shown that the cavity mode ordering and form of the standing wave functions are highly dependent on the point group symmetry of the mesa.

CHAPTER 2: LITERATURE REVIEW

BSCCO in the Context of Terahertz Radiation

$Bi_2Sr_2CaCu_2O_{8+\delta}$, also known as BSCCO-2212, is a type-II high-temperature superconductor of the cuprate family. The origin of BSCCO's interesting radiation properties is the layered nature of the material, as a unit cell consists of a superconducting layer of copper oxide sandwiched between two insulating layers consisting of bismuth oxide and strontium oxide. This crystal structure of BSCCO is shown in Figure 2.1, where the background indicates probability of electron occupancy.

When a DC Voltage is applied along the mesa, electrons will tunnel across the layers in Cooper pairs; that is, the periodicity of BSCCO gives rise to a stack of *intrinsic Josephson junctions* (IJJs). The relationship between applied voltage V_0 and frequency ω_J of the resulting AC Josephson current has been shown to satisfy $\omega_J = 2eV_0/\hbar N$, where N is the number of IJJs in the mesa [9]. In order to tune the emission frequency of the mesa, this DC voltage is varied along with the bath temperature of the mesa. It is this behavior of BSCCO as a stack of IJJs which gives rise to coherent emissions, and prevents effective modeling of the radiation mechanism by a simple dielectric cavity [8].

Early experiments showed that the IJJ stacks in BSCCO will radiate *synchronously* due to cavity mode resonance [10, 11]. The nonlinear portion of the AC Josephson current incited by the applied voltage will in fact lock on to one of the resonant cavity modes of the mesa which are intrinsic to the mesa geometry [8]. For a BSCCO mesa with N synchronously radiating junctions, the output power was proportional to N^2, partly explaining the reason why BSCCO mesas do not have significant power falloff centered around 1 THz as for some other solid-state emitters [12].

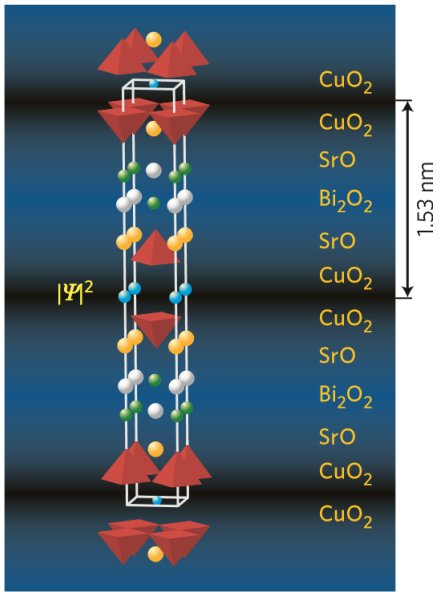

Figure 2.1: The crystal structure of $Bi_2Sr_2CaCu_2O_{8+\delta}$ [6].

Additionally, a BSCCO emitter will be operable at all temperatures below about 73 K, so the bath temperature serves as an additional mechanism for tuning the characteristic frequency of emission. Because BSCCO crystals with very high purity can be grown on the microscale and the IJJ mechanism for radiation is an intrinsic, compact source of coherent continuous wave emissions, BSCCO has seen a lot of attention with regards to THz research over the last decade [6].

The Dual Source Radiation Model

The radiation from a mesa of BSCCO at first glance appears difficult to accurately model due to the presence of free electric and magnetic currents in the bulk. Because BSCCO is a type-II layered superconductor, it possesses virtually no resistance, and these free currents will be persistent. On top of this, there is the additional effect of the AC Josephson current which is created by the static applied voltage, and is in principle nonlinear.

However, we show here that by modeling the AC Josephson current as two separable linear and nonlinear current density sources, and by taking advantage of the applicability of Love's equivalence principles to BSCCO (a perfect conductor below its critical temperature), the problem reduces to an application of the standard dual source radiation model in antenna theory [14].

In order to determine the output power of the radiation from a perfectly conducting source like BSCCO, one can find the combined intensity resulting from the superposition of an electric current density source $\boldsymbol{J}$ and a magnetic current density source $\boldsymbol{M}$ [15]. These current sources give rise to electric and magnetic fields $\boldsymbol{E}$ and $\boldsymbol{H}$, respectively, which are obtained via the auxiliary vector potentials $\boldsymbol{A}$ and $\boldsymbol{F}$.

For the specific case of a radiating BSCCO mesa, an applied DC voltage incites an AC Josephson current in the stack of IJJs. While this AC Josephson current is nonlinear, the dominating portion will be linear, so that a good approximation is to calculate the output power from the uniform and non-uniform portions separately. Then, we have for BSCCO a primary uniform source $\boldsymbol{J}$, and a secondary cavity mode current source $\boldsymbol{M}$. The uniform source is real and nonlinear, while the cavity mode source is linear and will lock on to one of the modes [8, 12]

Here, we follow [4, 14] by using Love's equivalence principles, which indicate that this problem is equivalent to one in which the emission is due to only the *surface* current density sources $\boldsymbol{J}_S$ and $\boldsymbol{M}_S$ [18]. Since the AC Josephson current travels parallel to the mesa boundary, we have transverse magnetic (TM) boundary conditions: the normal derivative of the magnetic field vanishes at the boundary.

The complete general description of this dual source antenna problem is determined by the set of electric and magnetic vector potentials, currents, and fields given in Table 2.1, where the relations between the vector potentials and the surface current densities are given by Equations 2.1 and 2.2. Following this prescription of putting all of the electric and magnetic source current emission onto

Table 2.1: Equations for the General Dual Source Radiation Problem

Current Source	Vector Potential	Electric Field	Magnetic Field
$\boldsymbol{J}_S$	$\boldsymbol{A}$	$\boldsymbol{E}_A = -\partial\boldsymbol{A}/\partial t$	$\boldsymbol{H}_A = \frac{1}{\mu}\nabla \times \boldsymbol{A}$
$\boldsymbol{M}_S$	$\boldsymbol{F}$	$\boldsymbol{E}_F = -\frac{1}{\epsilon}\nabla \times \boldsymbol{F}$	$\boldsymbol{H}_F = -\partial\boldsymbol{F}/\partial t$

the edges of the mesa yields the following for the magnetic and electric vector potentials [14],

$$\boldsymbol{A}(\boldsymbol{x}, t) = \frac{\mu_0}{4\pi} \int d^3\boldsymbol{x}' \boldsymbol{J}_S(\boldsymbol{x}', t) \frac{e^{ik_J R - i\omega_J t}}{R}, \tag{2.1}$$

$$\boldsymbol{F}(\boldsymbol{x}, t) = \frac{\epsilon_0}{4\pi} \int d^3\boldsymbol{x}' \boldsymbol{M}_S(\boldsymbol{x}', t) \frac{e^{ik_M R - i\omega_M t}}{R}, \tag{2.2}$$

where $R = |\boldsymbol{x} - \boldsymbol{x}'|$ is the distance from the source coordinates to the observation coordinates. The standard far field approximation $e^{ikR}/R \rightarrow e^{-i\mathbf{k}\cdot\mathbf{x}'}(e^{ikr}/r)$ may then be employed. Finally, the radiation intensity (i.e., the time average of the radiated power) will be

$$\frac{dP}{d\Omega} = \frac{1}{2} Re[r^2 \hat{r} \cdot \boldsymbol{E} \times \boldsymbol{H}^*] \tag{2.3}$$

However, one ambiguity which exists in solving the remainder of this problem is how to weight the contributions to the integrals along the boundary from each of the particular mesa edges. For some geometries such as the circular and equilateral triangular mesas, this is trivial. For the pie-shaped wedge, this is not the case, as simply giving each edge equal weighting (as in the case of the equilateral triangle) no longer limits to the bulk average. For this mesa geometry, then, determining a reasonable weighting scheme becomes a crucial first step.

CHAPTER 3: METHODOLOGY

Symmetry Considerations for the Equilateral Triangular Mesa

The TE and TM modes of the equilateral triangular waveguide have been determined theoretically in the past, but only the even modes were originally found [16, 17]. However, given that parity is a good quantum number for this waveguide geometry along the bisectors, it is clear that odd modes are also permitted; the wave functions for both are considered in [4], and are given by

$$\begin{aligned}\psi^{(e)}_{l,m,n} = &\cos\left[\left(\frac{2\pi x}{\sqrt{3}a}+\frac{2\pi}{3}\right)l\right]\cos\left[\frac{2\pi(m-n)y}{3a}\right]\\ &+\cos\left[\left(\frac{2\pi x}{\sqrt{3}a}+\frac{2\pi}{3}\right)m\right]\cos\left[\frac{2\pi(n-l)y}{3a}\right]\\ &+\cos\left[\left(\frac{2\pi x}{\sqrt{3}a}+\frac{2\pi}{3}\right)n\right]\cos\left[\frac{2\pi(l-m)y}{3a}\right],\end{aligned} \tag{3.1}$$

$$\begin{aligned}\psi^{(o)}_{l,m,n} = &\cos\left[\left(\frac{2\pi x}{\sqrt{3}a}+\frac{2\pi}{3}\right)l\right]\sin\left[\frac{2\pi(m-n)y}{3a}\right]\\ &+\cos\left[\left(\frac{2\pi x}{\sqrt{3}a}+\frac{2\pi}{3}\right)m\right]\sin\left[\frac{2\pi(n-l)y}{3a}\right]\\ &+\cos\left[\left(\frac{2\pi x}{\sqrt{3}a}+\frac{2\pi}{3}\right)n\right]\sin\left[\frac{2\pi(l-m)y}{3a}\right].\end{aligned} \tag{3.2}$$

In order for these wave functions to satisfy the wave equation $\nabla^2\psi + k^2\psi = 0$, the following relation must hold,

$$\begin{aligned} k_{l,m,n}^2 &= \left(\frac{2\pi}{3a}\right)^2 \left[(m-n)^2 + 3l^2\right] \\ &= \left(\frac{2\pi}{3a}\right)^2 \left[(n-1)^2 + 3m^2\right] \\ &= \left(\frac{2\pi}{3a}\right)^2 \left[(l-m)^2 + 3n^2\right]. \end{aligned} \tag{3.3}$$

Setting any two of these equations equal and factoring, we find that for the mode numbers

$$(n-m)(l+n+m) = 0, \tag{3.4}$$

where $l, m, n \in \mathbb{Z}^+$. Thus, there are *two* choices which will satisfy all three equations: (1) $l = -n - m$, or (2) $n = m$. Interestingly, the first of these was the only case investigated in [4, 17]. Here, case 2 will be considered. Requiring $n = m$ in Equation 3.3 fixes $l = n, -2n$. The choice $l = -2n$ is equivalent to the modes where $n = m$ in case 1.

However, for $l = m = n$ the resulting equation for k_n is not always degenerate with case 1, and we have $k_n = \sqrt{3n^2}$. Equations 3.1 and 3.2 with this choice of l reduce, respectively, to

$$\phi_n^{(e)} = 3\cos\left[\left(\frac{2\pi x}{\sqrt{3}a} + \frac{2\pi}{3}\right)n\right] \quad , \quad \phi_n^{(o)} = 0. \tag{3.5}$$

As $\phi_n^{(e)}$ is only a function in x, it will not satisfy the complete set of boundary conditions for any $n \in \mathbb{Z}^+$. So, this solution will *not* appear when the group symmetry is broken. Noting that this wave function satisfies just one of the boundary conditions, the natural choice is to rotate by 120° and 240° and superpose all three degenerate wave functions. The action of the ith rotation operator ρ_i in C_{3v} on an eigenfunction $\psi(x_0, y_0)$ of the Helmholtz equation in the boundary which is either

even or odd on reflection about the x_0 - axis is given by

$$\rho_i \psi(x_0, y_0) = \psi\left(\mathbf{r}_i\right) = \psi\left(J^{-i}\mathbf{r}_0\right), \tag{3.6}$$

where $\mathbf{r}_i$ is defined as the coordinate vector

$$\mathbf{r}_i \equiv \begin{pmatrix} x_i \\ y_i \end{pmatrix} = J^{-i} \begin{pmatrix} x_0 \\ y_0 \end{pmatrix} \tag{3.7}$$

and J is the Jacobian matrix for a clockwise rotation by 120° in Cartesian coordinates,

$$J = \begin{pmatrix} -\frac{1}{2} & \frac{\sqrt{3}}{2} \\ -\frac{\sqrt{3}}{2} & -\frac{1}{2} \end{pmatrix} \tag{3.8}$$

An equivalent process may be used to define a rotation in terms of the (x_1, y_1) or (x_2, y_2) coordinate bases. Given this, $\phi_n^{(e)}$ can be rotationally symmetrized (taking (x_k, y_k) as the coordinate basis, with $k \in \mathbb{Z}_3$) in the following manner:

$$\begin{aligned} \Phi_n^{(e)} &= \sum_{i=0}^{2} \phi_n^{(e)}(\mathbf{r}_i) = \sum_{i=0}^{2} \rho_i \phi_n^{(e)}(\mathbf{r}_k) = \sum_{i=0}^{2} \phi_n^{(e)}(J^{-i}\mathbf{r}_k) \\ &= 3\cos\left[\left(\frac{2\pi x_k}{\sqrt{3}a} + \frac{2\pi}{3}\right) n\right] + 6\cos\left[\left(\frac{2\pi}{3} - \frac{\pi x_k}{\sqrt{3}a}\right) n\right] \cos\left[\frac{n\pi y_k}{a}\right]. \end{aligned} \tag{3.9}$$

While this superposition satisfies the rotational symmetry of the triangle by construction, it may not satisfy the boundary conditions in general. On subjecting this C_{3v} symmetrized wave function to the full set of boundary conditions (see Appendix B), the result is that $\Phi_n^{(e)}$ will only satisfy the TM requirements on the entire boundary for *even* n. After restriction to even mode numbers, $\Phi_{2n}^{(e)}$

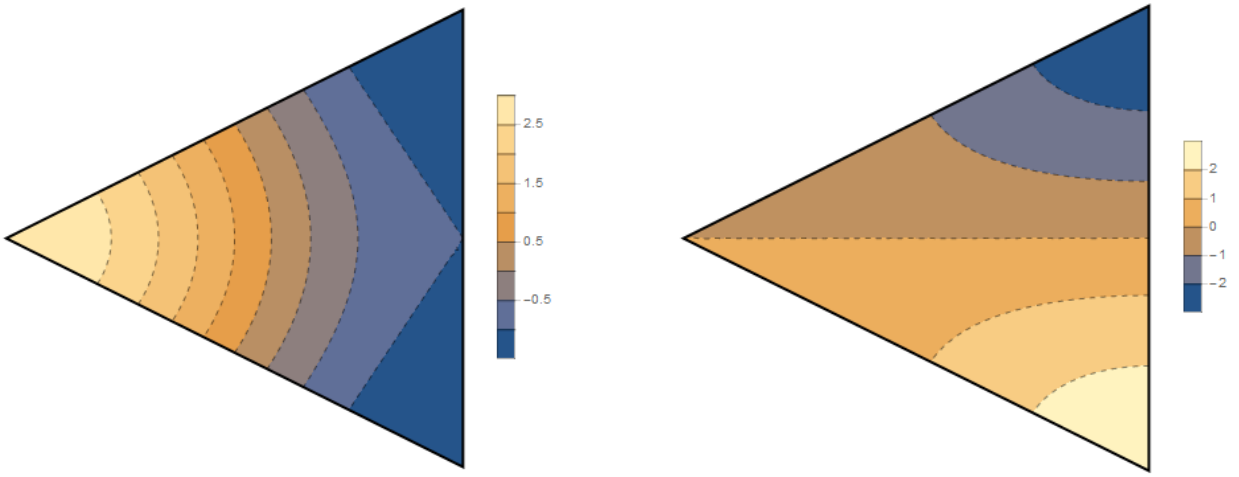

(a) (b)

Figure 3.1: Plots of the (a) even and (b) odd TM$(1,0)$ modes of the equilateral triangular mesa, which are degenerate ground state wave functions in the case of broken rotational symmetry.

is in fact identical to the original symmetric TM$(-2n,n,n)$ even modes up to a normalization,

$$\Phi_{2n}^{(e)} = 3\psi_{-2n,n,n}^{(e)}. \tag{3.10}$$

Thus, $l = -n - m$ is henceforth omitted from the mode characterizations without ambiguity, as the choice $l = m = n$ has been shown to provide no new eigenfunctions. It is shown in [4] that a rotation of the wave functions given in Equations 3.1 and 3.2 by $\pm 120^\circ$ with $l = -n - m$ will still satisfy the boundary conditions, necessitating a superposition of these degenerate wave functions for each even and odd TM(m,n) mode,

$$\Psi_{m,n}^{(e,o)} = \sum_{i=0}^{2} C_{m,n}^{i\,(e,o)} \psi_{m,n}^{(e,o)}(\mathbf{r}_i) \tag{3.11}$$

where the $C_{m,n}^{i\,(e,o)}$ are constants. This general description can be used to model the symmetry breaking effects of hot spots and defects (e.g. a linear mixture of the degenerate TM$(1,0)$ odd and

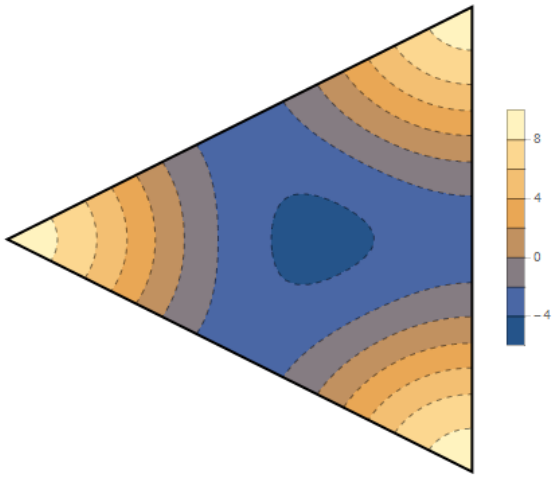

Figure 3.2: Diagram of the C_{3v} symmetric ground state for the equilateral triangular mesa.

even modes in Figure 3.1), but for an ideal mesa these constants $C_{m,n}^{i\,(e,o)}$ should be equal for a given even or odd TM(m,n) mode. Furthermore, in order for the cavity mode wave functions to be an orthonormal set, they must satisfy the rotational symmetry of the group [7]. We are thus motivated to examine as before the rotationally symmetrized wave functions

$$\Psi_{m,n}^{(e,o)} = \sum_{i=0}^{2} \rho_i \psi_{m,n}^{(e,o)}(\mathbf{r}_0) \tag{3.12}$$

When the odd and even wave functions are rotationally symmetrized, the only modes that do not vanish identically are those for which $m \equiv n$ (mod 3), with the additional restriction that $m \neq n$ for the odd wave functions. In fact, these are all of the terms in $\Psi_{l,m,n}^{(e,o)}$ for which there is preexisting rotational symmetry. Therefore, the admitted modes for an ideal equilateral triangular mesa are much sparser than in the case of the rotationally asymmetric solutions (Equations 3.1 & 3.2).

Strictly speaking, then, the ground state of the equilateral triangular mesa for TM boundary conditions is the TM$(1,1)$ mode. When rotational symmetry is broken by some local hot spot or defect, the odd and even TM$(1,0)$ modes (pictured in Figure 3.1) will be allowed, and the TM$(1,1)$ mode

is then the first excited state as presented in [17]. A plot of the C_{3v} symmetric TM$(1,1)$ ground state is given in Figure 3.2.

Some additional plots of the wave functions for the equilateral triangular mesa are given in Appendix A to illustrate the behavior of higher modes which satisfy the C_{3v} group symmetry when $m \neq n$.

Radiation Integrals for the Wedge Mesa

In the past, the edge integration for rectangular mesas was done by treating the mesa as a superposition of two perpendicular antennae by integrating in parallel directions along the length and width [8]. While this model gives fairly accurate results, it is clear that to properly implement Love's equivalence principle and obtain an accurate approximation to the volume average integration it is necessary to integrate in anti-parallel directions, i.e. to integrate in either a clockwise or counterclockwise direction around the parameter.

Table 3.1: Geometric Parameters for the Thin Wedge Mesa

a	b	ϕ_0	n_r
340 μm	90 μm	7.606°	4.2

In order to properly model the volume average integration as an edge integration using the Love equivalence principle, physical considerations suggest that the edges must be weighted with portions of the volume such that multiplying the separate edge weight factors recovers the total volume of the mesa. To illustrate this, in the case of the pie-shaped wedge (which may be represented as in Figure 3.3, using Table 3.1), the uniform electric AC Josephson current source along the edges

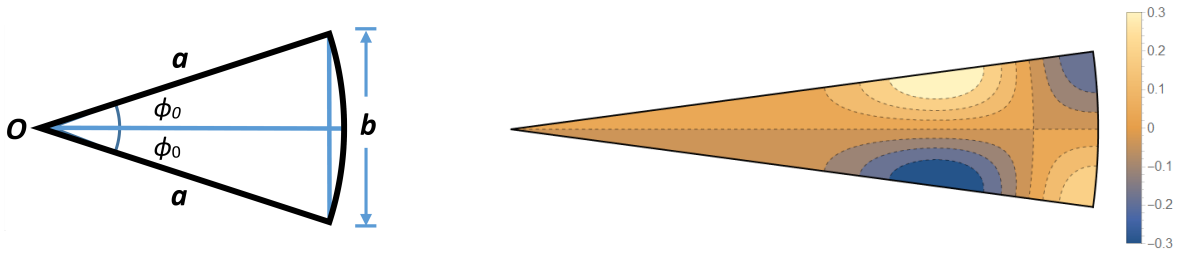

(a) (b)

Figure 3.3: (a) Diagram of the wedge model for an isosceles triangular mesa, and (b) the TM$(2,0)$ odd wave function used to fit the acute isosceles triangular mesa emission data.

can be written as

$$\boldsymbol{J}_S(\boldsymbol{x}',t) = \hat{\boldsymbol{z}}'\eta(z')J_J e^{-i\omega_J t}\frac{1}{2}\left[\alpha\delta(\rho'-a)\Theta(\phi_0^2-\phi'^2)+\beta\frac{\Theta(a-\rho')}{\rho'}\sum_{\sigma=\pm}\sigma\delta(\phi'+\sigma\phi_0)\right], \quad (3.13)$$

where the terms α and β will weight the integrals along the arc and the sides of the wedge parameter, respectively. The power can be determined via integration of this surface current density using Equation 2.1. However, the result of this integration is dependent on whether the volume average approximation or edge integration technique is used, so a closed form for the power will not be given. The weighting scheme for Equation 3.13 which seems most physically reasonable is to take

$$\alpha = a,\ \beta = a\phi_0 \ \Rightarrow\ \alpha\beta = a^2\phi_0 = v, \quad (3.14)$$

such that the product of the weighting factors recovers the volume of the wedge. This is the weighting scheme which I will employ in investigating the radiation intensity profile for the pie-shaped wedge mesa. Given this choice of weights, using Table 2.1 for the magnetic current source,

$$\begin{aligned}\boldsymbol{M}_{\nu_n^{(o,e)}}(\rho',\phi',z') =& \frac{\partial A_{z,\nu_n^{(o,e)}}(\boldsymbol{x}',t)}{\partial t}\eta(z')\frac{a}{2}\left[\hat{\boldsymbol{\phi}}'\phi_0\delta(\rho'-a)\Theta(\phi_0^2-\phi'^2)\right.\\ &\left.+\sum_{\sigma}\hat{\boldsymbol{\rho}}'\sigma\phi_0\delta(\phi'+\sigma\phi_0)\frac{\Theta(a-\rho')}{\rho'}\right],\end{aligned} \tag{3.15}$$

$$A_{z,\nu_n^{(o)}}(\rho',\phi',z') = C_{\nu_n^{(o)}}\sin(\nu_n^{(o)}\phi')J_{\nu_n^{(o)}}(k\rho')\frac{e^{i(kr-\omega t)}}{r}e^{-i\boldsymbol{k}\cdot\boldsymbol{x}'}, \tag{3.16}$$

$$A_{z,\nu_n^{(e)}}(\rho',\phi',z') = C_{\nu_n^{(e)}}\cos(\nu_n^{(e)}\phi')J_{\nu_n^{(e)}}(k\rho')\frac{e^{i(kr-\omega t)}}{r}e^{-i\boldsymbol{k}\cdot\boldsymbol{x}'}, \tag{3.17}$$

where $J_{\nu_n^{(o,e)}}$ are non-integral Bessel functions of the first kind, $C_{\nu_n^{(o,e)}}$ are the mode amplitude constants, $\sin(\nu_n^{(o)}\phi') = \sin\left[\left(n+\frac{1}{2}\right)\frac{\pi\phi'}{\phi_0}\right]$, $\cos(\nu_n^{(e)}\phi') = \cos\left[\frac{n\pi\phi'}{\phi_0}\right]$, and the $A_{z,\nu_n^{(o,e)}}(\rho',\phi',z')$ are the wave function amplitudes for the cavity mode emissions. These wave functions have already been found for many of the odd and even $\mathrm{TM}(m,n)$ modes of the pie-shaped wedge model for acute isosceles triangular mesas [4, 5]. The electric vector potential is determined separately from $\boldsymbol{M}_{\nu_n^{(o,e)}}(\rho',\phi',z')$ for the odd and even cavity modes using Equation 2.2 by integrating along the edges of the mesa,

$$\begin{aligned}\boldsymbol{F}_{\nu_n^{(o)}}(\boldsymbol{x},t) =& \frac{-i\omega\epsilon_0 e^{i(kr-\omega t)}C_{\nu_n^{(o)}}}{2\pi r}\frac{ha}{2}\left(\phi_0\int_0^a d\rho'\left(\hat{\boldsymbol{\theta}}\cos\theta\cos(\phi+\phi_0)-\hat{\boldsymbol{\phi}}\sin(\phi+\phi_0)\right)\right.\\ &\times\left[e^{-ik\rho'\sin\theta\cos(\phi+\phi_0)}\sin(-\nu_n^{(o)}\phi_0)J_{\nu_0^{(o)}}(k\rho')\right]\\ &+a\int_{-\phi_0}^{\phi_0}d\phi'\left(\hat{\boldsymbol{\theta}}\cos\theta\sin(\phi-\phi')+\hat{\boldsymbol{\phi}}\cos(\phi'-\phi)\right)\\ &\times\left[e^{-ika\sin\theta\cos(\phi-\phi')}\sin(\nu_n^{(o)}\phi')J_{\nu_0^{(o)}}(ka)\right]\\ &+\phi_0\int_a^0 d\rho'\left(\hat{\boldsymbol{\theta}}\cos\theta\cos(\phi-\phi_0)-\hat{\boldsymbol{\phi}}\sin(\phi-\phi_0)\right)\\ &\left.\times\left[e^{-ik\rho'\sin\theta\cos(\phi-\phi_0)}\sin(\nu_n^{(o)}\phi_0)J_{\nu_0^{(o)}}(k\rho')\right]\right),\end{aligned} \tag{3.18}$$

$$
\begin{aligned}
\boldsymbol{F}_{\nu_n^{(e)}}(\boldsymbol{x},t) =& \frac{-i\omega\epsilon_0 e^{i(kr-\omega t)} C_{\nu_n^{(e)}}}{2\pi r}\frac{ha}{2}\left(\phi_0\int_0^a d\rho'\left(\hat{\boldsymbol{\theta}}\cos\theta\cos(\phi+\phi_0)-\hat{\boldsymbol{\phi}}\sin(\phi+\phi_0)\right)\right.\\
&\times\left[e^{-ik\rho'\sin\theta\cos(\phi+\phi_0)}\cos(-\nu_n^{(e)}\phi_0)J_{\nu_0^{(e)}}(k\rho')\right]\\
&+a\int_{-\phi_0}^{\phi_0}d\phi'\left(\hat{\boldsymbol{\theta}}\cos\theta\sin(\phi-\phi')+\hat{\boldsymbol{\phi}}\cos(\phi'-\phi)\right)\\
&\times\left[e^{-ika\sin\theta\cos(\phi-\phi')}\cos(\nu_n^{(e)}\phi')J_{\nu_0^{(e)}}(ka)\right]\\
&+\phi_0\int_a^0 d\rho'\left(\hat{\boldsymbol{\theta}}\cos\theta\cos(\phi-\phi_0)-\hat{\boldsymbol{\phi}}\sin(\phi-\phi_0)\right)\\
&\times\left.\left[e^{-ik\rho'\sin\theta\cos(\phi-\phi_0)}\cos(\nu_n^{(e)}\phi_0)J_{\nu_0^{(e)}}(k\rho')\right]\right).
\end{aligned}
\tag{3.19}
$$

The power can then be found by simply grouping the θ and ϕ components of the odd and even vector potentials,

$$
\frac{dP_{\nu_n^{(o,e)}}}{d\Omega}\propto|\bar{F}_{\nu_n^{(o,e)},\theta}|^2\cos^2\theta+|\bar{F}_{\nu_n^{(o,e)},\phi}|^2. \tag{3.20}
$$

To determine the angular dependence of the radiation intensity profiles for the pie-shaped wedge mesa requires numerical calculation; the integrals involved in computing the power contributions from both the uniform AC Josephson current and the cavity mode sources cannot be evaluated analytically. For the cavity modes, it will be necessary to evaluate zeros of the derivatives of the non-integral Bessel functions $J_{\nu_n^{(o,e)}}$. These values are numerically known, and have been given in [4, 5]. The Bessel zero which corresponds to the TM$(2,0)$ odd mode to be fit is $\chi(2,\nu_0^o)\approx 18.55$.

As the emission data to be fit with the wedge model was measured for a mesa on a substrate, an additional factor of $\cos^2\theta$ is included in the formulas for the power contributions from the uniform and cavity mode sources. This substrate factor is shown to accurately model the effects of the substrate on the angular emission spectrum [8].

A Brief Discussion of the Integration Weighting Factors

The proposed weighting scheme seems to be the most physically logical choice, and behaves in the limits of the very thin and nearly circular wedge. However, it is still only an approximation to the volume average, and will deviate from it for intermediate central angles and thus for cases such as the semicircular mesa.

Despite this, such a choice of weighting factors for edge integration using Love's equivalence principles is necessary for numerical calculation of the cavity mode radiation profiles due to the magnetic current source, as volume average techniques in this case present difficult ambiguities. Namely, volume average integration for the magnetic current source entails directional integration along the surface of the mesa, but it is unclear how to divide the area into regions which specify a clockwise or counterclockwise flow of integration.

Arbitrary division of the wedge into three regions such that each can be seen as analogous to integration along the neighboring edge of the region is not physically justifiable unless proper division of the area is accounted for. At a glance, it would seem that division into three regions by the center of mass gives the desired result, but this scheme breaks down at larger central angles.

Furthermore, there is no way to allow for smooth boundaries between the integration regions for the case of a semicircular mesa, nor for any wedge with central angle larger than this. Thus, the discussed weighting factors of a for the arc integral and $a\phi_0$ for the edge integrals will be used both for calculation of the radiation intensity from the uniform portion of the AC Josephson current and for the angular dependence of the cavity mode radiation emissions.

CHAPTER 4: RESULTS

Numerical Evaluation of the Uniform Source Integral for the Wedge Mesa

Numerical results for the edge integration of the intrinsic Josephson junction emission portion using the proposed weighting factors in Equation 3.14 are compared with the volume average integration in Figure 4.1. Here the wedge dimensions used are those of sample four in [5], detailed in Table 3.1.

While the two integration techniques give similar results, the edge integration method appears to rotate the angular intensity plot by an angle ϕ_0. Therefore, this edge weighting scheme will deviate from the volume average when the central angle is large.

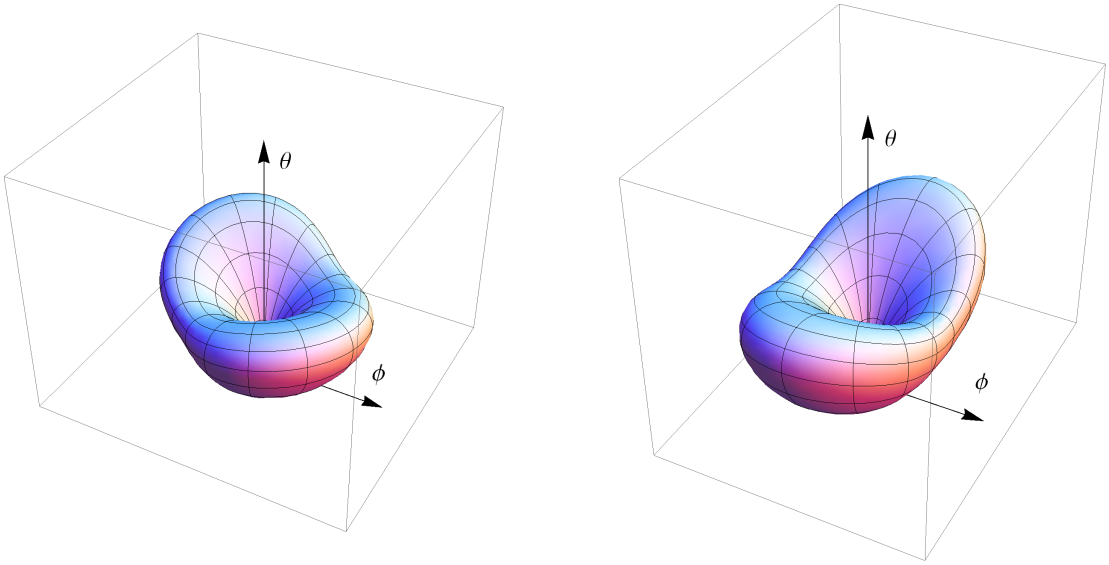

(a) (b)

Figure 4.1: Plots of the uniform source contribution for the TM(2,0) odd mode of the thin wedge mesa using (a) the edge integration method and (b) the volume average approximation.

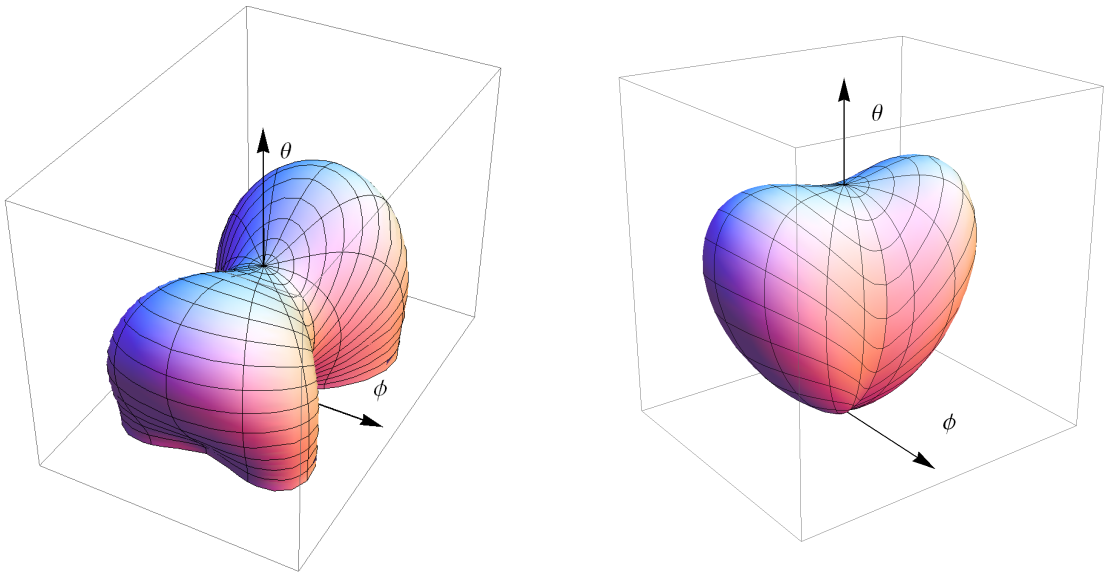

(a) (b)

Figure 4.2: Plots of the cavity mode power contribution for the TM$(2,0)$ odd mode of the thin wedge mesa where a substrate factor has been (a) omitted (b) included.

Numerical Evaluation of the Cavity Mode Integrals for the Wedge Mesa

The results of the numerical integration of the TM$(2,0)$ odd cavity mode integrals are shown in Figure 4.2. To illustrate the large effect the substrate has on the angular dependence of the intensity, the results with and without a substrate factor are given; the latter will be used in fitting the experimental data for the acute isosceles triangular mesa.

Fitting of Experimental Data for the Isosceles Triangular Mesa by the Wedge Model

Figure 4.4 shows the result of the two parameter least-squares fit of the emission data with the wedge model using the edge integration technique for the cavity mode radiation. In this case, the resulting fit has a standard deviation $\sigma = 0.4657$. In comparison, the fit given in Figure 4.5 uses

the volume average integration technique for gives a larger standard deviation of $\sigma = 0.4894$. This empirically confirms the choice of weighting factors detailed in Chapter 3.

It should be noted that the resulting best fit to the data has coefficients such that the contributions to the total power of the uniform Josephson and cavity mode sources are comparable. However, the uniform contribution dominates slightly in the fit to the data, as the TM$(2, 0)$ cavity mode does not possess sufficient anisotropy to adequately fit the data in the xz-plane and yz-plane simultaneously well.

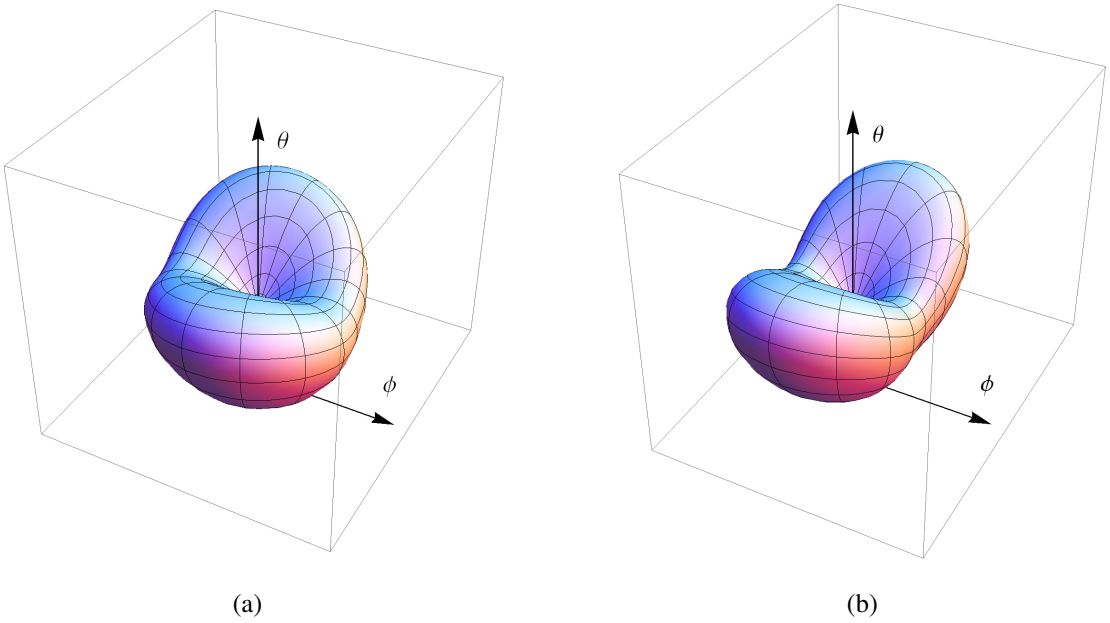

(a) (b)

Figure 4.3: Plots of the total radiation power emitted for the acute isosceles triangular mesa (sample 4) in [4, 5] using a least-squares fit by the dual source radiation model. To numerically evaluate the uniform AC Josephson junction contribution, the (a) edge integration method and (b) volume average approximation have been used.

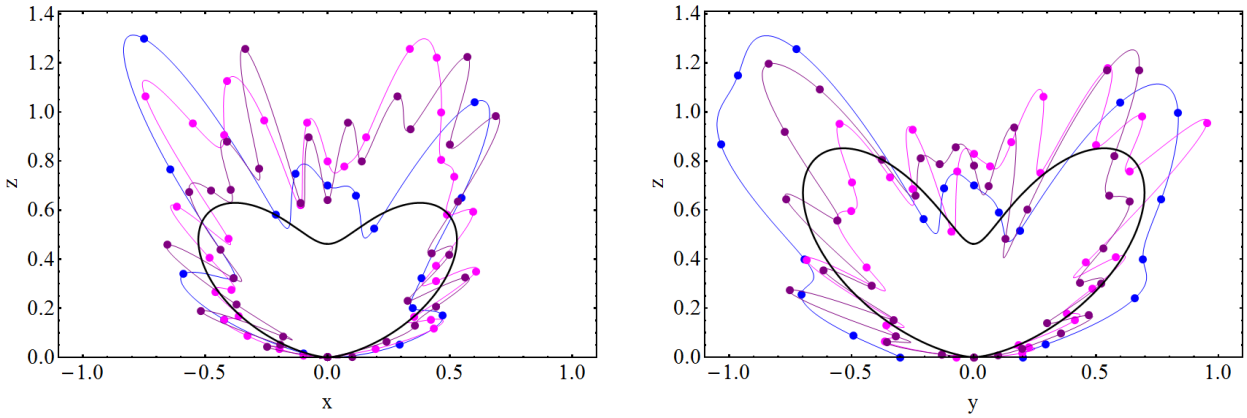

(a) (b)

Figure 4.4: Plots of experimental data and the least-squares fit (black) for $\mathcal{I}(\theta, \phi)$ for the acute isosceles triangular mesa in the (a) xz and (b) yz planes, where the edge integration method has been implemented for the uniform source contribution.

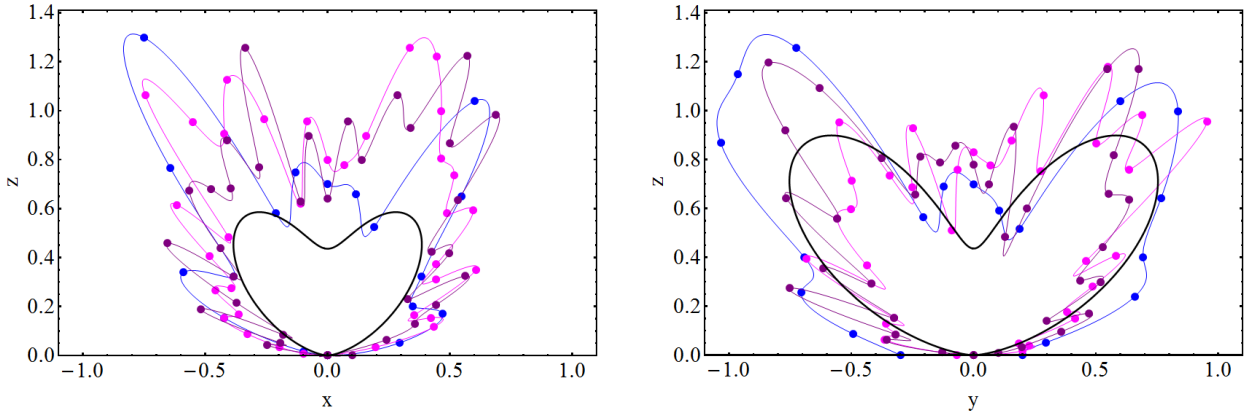

(a) (b)

Figure 4.5: Plots of experimental data and the least-squares fit (black) for $\mathcal{I}(\theta, \phi)$ for the acute isosceles triangular mesa in the (a) xz and (b) yz planes using the volume average approximation for the uniform source integrals.

CHAPTER 5: CONCLUSION

The geometry of superconducting BSCCO mesas has been shown to play a large role in the nature of THz emission from these devices. Specifically, the point group symmetry of the mesa has a drastic effect on the cavity mode wave function distribution of the equilateral triangle. The original ground state wave function vanishes upon rotational symmetrization, leaving the TM$(1,1)$ even mode as the true C_{3v} symmetric ground state. Earlier experiments on the position of the voltage bias on a pentagonal mesa and its drastic effect on the emission frequency suggest that symmetry breaking effects can be used for tuning purposes as well [3]. Future work should be done with regards to developing a phenomenological model of the mesa quality with respect to hot spot, sample defect, and surface effects, in attempts to quantify the symmetry breaking.

For the acute isosceles triangular mesa, the pie-shaped wedge model has been shown to provide a good approximation to experimental data for the angular dependence of emission intensity. In this case, the edge integration technique for the uniform portion of the AC Josephson current fit the data better, with a standard deviation of $\sigma = 0.4657$ as opposed to the slightly higher $\sigma = 0.4894$ for the volume average approximation. Therefore, the approximation of the acute isosceles triangular mesa by a pie-shaped wedge appears well-founded and quite accurate. It is possible that the edge integration method with weights given by Equation 3.14 will not in general fit the data better, and it remains to be seen whether or not this will be consistent for other choices of central angle ϕ_0.

APPENDIX A: EQUILATERAL TRIANGLE WAVE FUNCTIONS

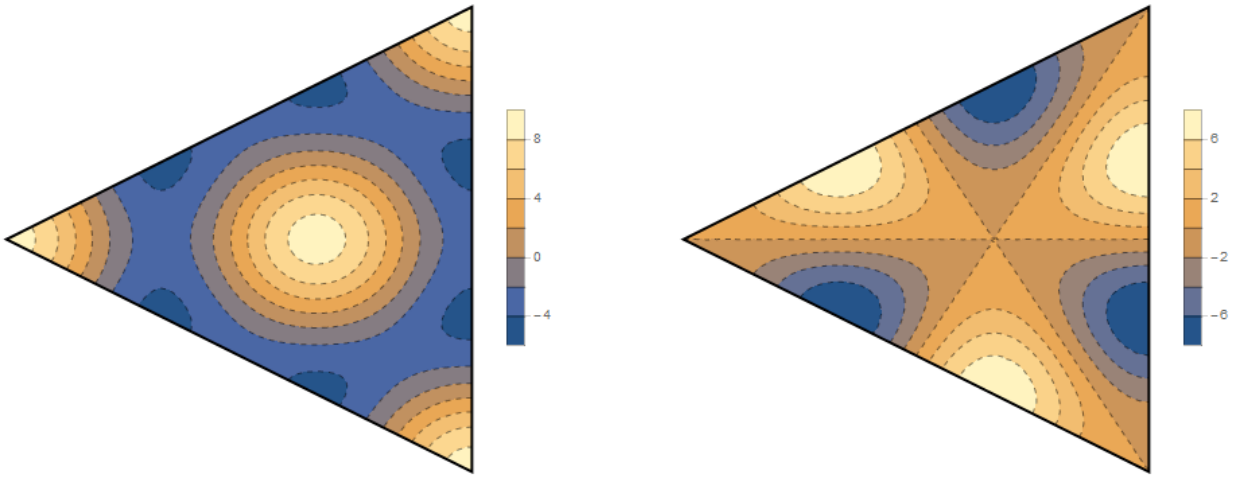

(a) (b)

Figure A.1: Plots of the (a) even and (b) odd TM$(3, 0)$ modes of the equilateral triangular mesa.

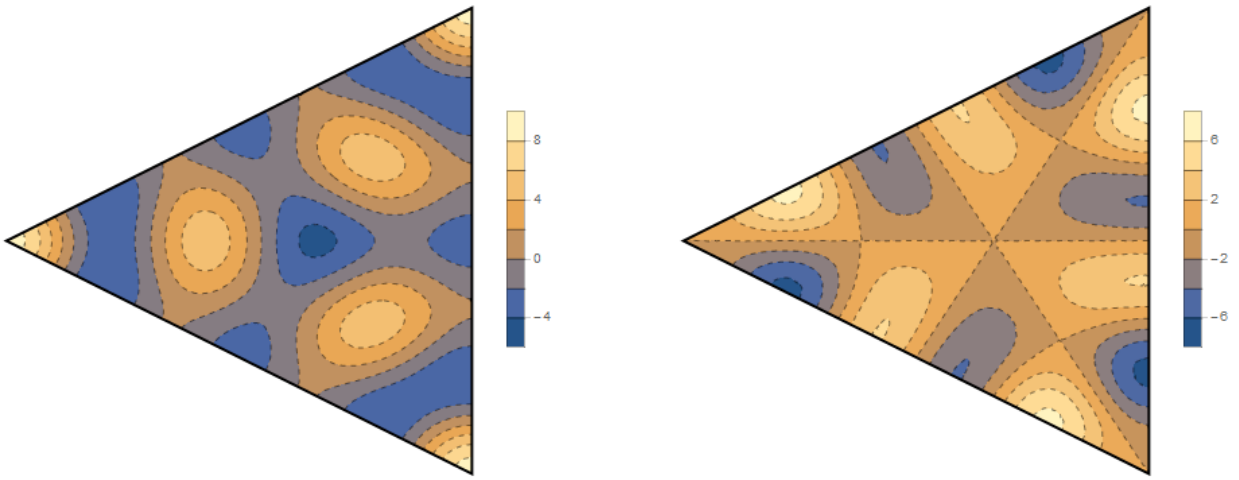

(a) (b)

Figure A.2: Plots of the (a) even and (b) odd TM$(4, 1)$ modes of the equilateral triangular mesa.

APPENDIX B: BOUNDARY CONDITIONS FOR THE EQUILATERAL TRIANGLE

The set of TM boundary conditions for the equilateral triangle are C_{3v} symmetric pure Neumann boundary conditions, i.e., the set of equations

$$\left.\frac{\partial\psi(x_i,y_i)}{\partial x_i}\right|_{x_i=a/(2\sqrt{3})}=0 \tag{B.1}$$

is symmetric about coordinate rotations of $\pm 120^\circ$, where $i=0,1,2$. From Equation 3.9, for the rotationally symmetrized even wave functions with $l=m=n$:

$$\Phi_n^{(e)}=3\cos\left[\left(\frac{2\pi x_i}{\sqrt{3}a}+\frac{2\pi}{3}\right)n\right]+6\cos\left[\left(\frac{2\pi}{3}-\frac{\pi x_i}{\sqrt{3}a}\right)n\right]\cos\left[\frac{n\pi y_i}{a}\right]. \tag{B.2}$$

Applying Equation B.1 to $\Phi_n^{(e)}$ then gives

$$\begin{aligned}\left.\frac{\partial\Phi_n^{(e)}}{\partial x_i}\right|_{x_i=\frac{a}{2\sqrt{3}}} &= \frac{2\sqrt{3}n\pi}{a}\left\{\sin\left[\left(\frac{2\pi}{3}-\frac{\pi x_i}{\sqrt{3}a}\right)n\right]\cos\left[\frac{n\pi y_i}{a}\right]-\sin\left[\left(\frac{2\pi}{3}+\frac{\pi x_i}{\sqrt{3}a}\right)n\right]\right\}_{x_i=\frac{a}{2\sqrt{3}}}\\ &= \frac{2\sqrt{3}n\pi}{a}\left\{\sin\left(\frac{n\pi}{2}\right)\cos\left(\frac{n\pi y_i}{a}\right)-\sin\left(n\pi\right)\right\}\\ &= \begin{cases}0, & n \text{ even},\\ \frac{2\sqrt{3}n\pi}{a}\cos\left(\frac{n\pi y_i}{a}\right)(-1)^{n-1}, & n \text{ odd},\end{cases}\end{aligned} \tag{B.3}$$

which is not identically zero for all y_i on the boundary. Therefore, in order for $\Phi_n^{(e)}$ to satisfy the boundary conditions, we must restrict ourselves to even values of n.

LIST OF REFERENCES

[1] T. Kashiwagi, K. Sakamoto, H. Kubo, Y. Shibano, T. Enomoto, T. Kitamura, K. Asanuma, T. Yasui, C. Watanabe, K. Nakade *et al.*, Appl. Phys. Lett. **107**, 082601 (2015).

[2] T. Kashiwagi, T. Yamamoto, T. Kitamura, K. Asanuma, C. Watanabe, K. Nakade, T. Yasui, Y. Saiwai, Y. Shibano, H. Kubo *et al.*, Appl. Phys. Lett. **106**, 092601 (2015).

[3] K. Delfanazari, H. Asai, M. Tsujimoto, T. Kashiwagi, T. Kitamura, T. Yamamoto, W. Wilson, R. A. Klemm, T. Hattori, K. Kadowaki, IEEE Trans. Terahertz Sci. Technol. **5**(3), 505 (2015).

[4] R. A. Klemm, K. Delfanazari, M. Tsujimoto, T. Kashiwagi, T. Kitamura, T. Yamamoto, M. Sawamura, K. Ishida, T. Hattori, and K. Kadowaki, Physica C **491**, 30 (2013).

[5] K. Delfanazari, H. Asai, M. Tsujimoto, T. Kashiwagi, T. Kitamura, T. Yamamoto, M. Sawamura, K. Ishida, C. Watanabe, S. Sekimoto *et al.*, Opt. Express **21**, 2171 (2013).

[6] U. Welp, K. Kadowaki, and R. Kleiner, Nat. Photonics **7**, 702 (2013).

[7] N. Stambaugh and M. Semon, Can. J. Phys. **99**, 1 (2013).

[8] R. A. Klemm and K. Kadowaki, J. Phys.: Condens. Matter **22**, 375701 (2010).

[9] R. A. Klemm and K. Kadowaki, J. Supercond. Nov. Magn. **23**, 613 (2010).

[10] H. B. Wang, S. Gunon, J. Yuan, A. Iishi, S. Arisawa, T. Hatano, T. Yamashita, D. Koelle, and R. Kleiner, Phys. Rev. Lett. **102**, 017006 (2009).

[11] K. Kadowaki, H. Yamaguchi, K. Kawamata, T. Yamamoto, H. Minami, I. Kakeya, U. Welp, L. Ozyuzer, A.E. Koshelev, C. Kurter *et al.*, Physica C **468**, 634 (2008).

[12] L. Ozyuzer, A. E. Koshelev, C. Kurter, N. Gopalsami, Q. Li, M. Tachiki, K. Kadowaki, T. Yamamoto, H. Minami, H. Yamaguchi, T. Tachiki, K. E. Gray, W.-K. Kwok, U. Welp, Science **318**, 1291 (2007).

[13] B. Williams, Nature Photonics **1**, 517 (2007).

[14] C. A. Balanis, *Antenna Theory: Analysis and Design*, 3rd Ed. (Wiley, Hoboken, NJ, 2005).

[15] J. D. Jackson, *Classical Electrodynamics*, 3rd Ed. (Wiley, New York, NY, 1999).

[16] P. L. Overfelt and D. J. White, IEEE Trans. Microwave Theory Tech. **34**(1), 161 (1986).

[17] J. Helszajn and D. S. James, IEEE Trans. Microwave Theory Tech. **26**(2), 95 (1978).

[18] A. E. H. Love, Phil. Trans. R. Soc. A **197**, 1 (1901).